Characteristic analysis of lithium–oxygen batteries considering the discontinuous deposit and electrolyte degradation effects during discharge

Wei Li[a] *, Min Zeng[b], Bonghong Wang[c], Yujie Chen[d], Christos N. Markides[e]

[a] Jiangsu Key Laboratory of Process Enhancement and New Energy Equipment Technology, School of Mechanical and Power Engineering, Nanjing Tech University, Nanjing, 211816, China

[b] Key Laboratory of Thermo–Fluid Science and Engineering, Ministry of Education, Xi'an Jiaotong University, Xi'an, Shaanxi, 710049, China

[c] National & Local Joint Engineering Research Center of Harbor Oil & Gas Storage and Transportation Technology, Zhejiang Ocean University, No.1 Haida South Road, Zhoushan 316022, PR China

[d] School of Mechanical Engineering, Beijing Institute of Petrochemical Technology, Beijing, 102617, China

[e] Clean Energy Processes (CEP) Laboratory, Department of Chemical Engineering, Imperial College London, London SW7 2AZ, UK

* E-mail address: wli@njtech.edu.cn (W. Li)

N.B.: This is the ACCEPTED MANUSCRIPT version of this article. The final, published version of the article can be found at: https://doi.org/10.1016/j.est.2024.110544

ABSTRACT

The modeling research plays a crucial role in grasping the reaction mechanisms and forecasting the performance of lithium-oxygen (Li–O_2) batteries. A transient Li-O_2 battery model including continuity, transportation, and reaction kinetics by simultaneously considering the discontinuous deposit of discharge product Li_2O_2 and the formation of by-product Li_2CO_3 due to electrolyte degradation, is developed to reveal the discharge phenomena. The effects of operating conditions and electrolyte and electrode properties on the discharge behaviors including voltage-capacity curve, energy density, profiles of O_2 concentration (C_{O2}) and porosity (ε) at the cathode are quantitatively studied. It is found that enhancing O_2 solubility (S_{O2}) and diffusivity (D_{O2}) significantly improves discharge capacity and voltage plateau; the promotion of voltage plateau will be inconspicuous as electrolyte conductivity (κ) is enlarged over 1 S/m. With the rise of ε from 0.73 to 0.93, the specific capacity is boosted from 874 to 6122 mAh/$g_{\text{-carbon}}$, and the corresponding specific energy upgrades from 2260 to 15610 mWh/$g_{\text{-carbon}}$. Shortening cathode thickness (L_{ca}) facilitates the efficient utilization of carbon cathode material but this comes at the expense of lowering the mass loading of carbon, the practical energy drops 59.4% as L_{ca} reduces from 750 μm to 100 μm. After 20 consecutive charge-

discharge cycles, the capacity retention obtained is 36.884%, accompanied by a 13.8% volume fraction of Li_2CO_3 formation inside the cathode. This work may guide in designing electrodes and electrolytes and provide performance regulation strategies for Li-O_2 batteries.

Keywords: Li–O_2 batteries; Discharge behaviors; Porous cathode; Deposit layer; Electrolyte degradation

Nomenclature

a	specific surface area (m^2/m^3)
b	Bruggeman factor
C	concentration of species (mol/m^3)
D	gas diffusivity (m^2/s)
Da	Damköhler number
d	distance (m)
E	potential (V)
F	Faraday constant (96,485 C/mol)
i	current density (A/m^2)
I_{app}	applied current density (A/m^2)
j	interfacial transfer current density (A/m^2)
k	reaction rate constant
L	Thickness (m)
M	molar mass (kg/mol)
n	number of electrons transported
p	geometric factor
R	ideal gas constant (J/mol/K)
R_{Li2O2}	electrical resistivity across Li_2O_2 film formation (Ω/m^2)
r	Radius (m)
S	reaction rate ($mol/m^3/s$)
S_{O2}	solubility factor of O_2
s	stoichiometric coefficient
T	temperature (K)
t	time (s)
t_+	transference number of cation in electrolyte
z	charge number of Li^+

Greek symbols

ρ	density (kg/m^3)
β	symmetry factor
γ	geometric factor
μ	geometric factor
θ	Li_2O_2 surface coverage
ε	porosity or volume fraction
η	overpotential (V)
κ	ionic conductivity (S/m)
δ	deposit layer thickness (m)
σ	electronic conductivity (S/m)
Φ	electric potential (V)

Subscripts

0	initial
a	anode
app	applied
ca	cathode
DL	deposit layer
eff	effective
i	species
l	liquid phase
max	maximum
O_2	oxygen
s	solid phase

Abbreviations

APL	anode protective layer
CDL	continuous deposit layer
DDL	discontinuous deposit layer
EES	electrochemical energy storage
ESD	energy storage density
ORR	oxygen reduction reaction
SOC	state of charge
SOD	state of discharge

1

1. Introduction

In 2021 global energy-related CO_2 emissions reached 33 Gt with a growth of 4.8%, returning to pre-pandemic levels as demand for coal, oil, and gas rebounded with the economy [1]. The overreliance of current civilization on fossil fuels, constituting over 80% of the primary energy sources globally, represents a compelling challenge to climate degradation and environmental risks [2]. Efforts have been underway in recent years to foster an energy revolution, shifting from carbon-based sources to inexhaustible renewables [3]. This aims to diminish reliance on fossil fuels and minimize carbon emissions.

On the other hand, the widespread utilization of renewable energies, despite their considerable potential, is hindered by various factors including intermittence and spatial-temporal dependence, leading to a disparity between energy supply and demand [4]. Electrochemical energy storage (EES) equipment is a key component in the future energy network to smooth out the erratic energy production and supply from renewables [5]. Among these potential EES candidates, metal−air (oxygen) batteries have garnered significant interest in the past two decades. Lithium-oxygen (Li-O_2) batteries exhibit an ultra-high theoretical specific energy storage density (ESD) of 11400 Wh/kg (3500 Wh/kg based on Li and O_2), which is far greater than that of other aqueous and non-aqueous metal−air batteries, as presented in Fig. 1. The comparable ESD to that of gasoline fuel (13000 Wh/kg) promise it an alternative for lithium-ion batteries in electric vehicle application. Although the rechargeable Li-O_2 battery provides extremely high theoretical ESD, some severe challenges faced such as its poor cyclability and species transport capability, make it still stay in the lab research stage [6,7].

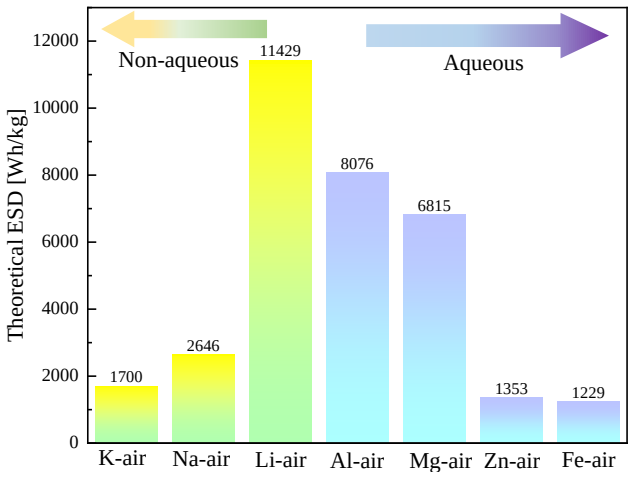


Fig. 1. Theoretical ESDs for different types of metal-air batteries.

To enhance the reaction kinetics of oxygen reduction reaction for Li_2O_2 formation during discharge and oxidation reaction for Li_2O_2 decomposition during charge, Kim et al. [8] prepared bifunctional catalysts consisting of pyrochlore $LaSrSn_2O_7$ nanoparticles and one-dimensional carbon nanofibers, the results indicated that a good cyclability of the cathode was realized over 54 cycles with a low overpotential when operated at a rate of 200 mA/g, achieving a specific capacity of 500 mAh/g. By intelligently regulating the electronic structure of platinum/vanadium oxide (Pt/VO_x), Dou et al. [9] reached the satisfying catalysis for the bidirectional electrode process, and Li–O_2 battery with Pt/VO_x electrodes exhibit ultra-low charge overpotential (0.14 V) and higher capacity (13270 mAh/g). To provide high catalytic activity, Lv et al. [10] systematically developed a chromium-doped Mn_3O_4 electrocatalyst to produce abundant oxygen vacancies. They found the optimized electrode exhibited low overpotential and high specific capacity, accompanied by excellent rate performance and stable cycle. Wang et al. [11] utilized nickel-based heterostructures as catalysts, and it was found because of the synergistic effect of heterostructures, the ESD, round-trip efficiency, and cyclability of Li-O_2 batteries were improved. Other high-performance heterogeneous catalysts [12–15], homogeneous catalysts [16–18], as well as functional additives [19–21], have also been synthesized to promote the generation and decomposition of products.

In recent research, Kondori et al. developed a composite polymer electrolyte based on $Li_{10}GeP_2S_{12}$ nanoparticles dispersed in a modified polyethylene oxide polymer matrix, they reported the improved Li-O_2 battery is rechargeable for 1000 cycles with a low polarization gap and can operate at high rates [22]. By employing 2D titanium carbonitride and 3D reduced graphene oxide-based conductive scaffold architecture to regulate Li nucleation and solid-electrolyte interphase (SEI), superior cycling over 900 cycles of Li metal batteries can be ensured [23]. Similarly, some efficient artificial SEI [24,25] and oxygen-selective membranes [26,27] were developed for reaching long-term stability of Li-O_2 batteries. Besides, several novel electrolyte and electrode systems have been proposed to boost the sustainable operation of redox-mediated Li-O_2 batteries [28–31].

In addition to preparing the new materials for Li-O_2 batteries' performance enhancement, several modeling studies regarding Li-O_2 batteries have also been conducted. Sahapatsombut et al. [32,33] reported a micro-macro homogeneous mathematical model for Li-O_2 batteries based on the concentrated binary electrolyte theory, and the dynamic behaviors of the porous cathode considering Li_2O_2 as a discharge product were numerically

analyzed. Gwak and Ju [34] used a 3D transient model to evaluate the Li_2O_2 formation and growth in an air electrode, as well as the electrochemical reactions and species transport during discharge. Tan et al. [35] numerically investigated the influences of electrolyte and electrode properties on discharge performance with LiO_2 as the discharge product. Jung et al. [36] numerically demonstrated that treating the discharge product of Li_2O_2 as a discontinuous deposit layer could more precisely predict the product formation on carbon surfaces, especially in the case of low discharge current.

It is clear from the review above that published papers primarily focused on two orientations: 1) The development of novel catalysts, including preparation, characterization, elucidation of reaction mechanisms, and performance adjustment. 2) Improving mass transport by designing and optimizing SEI, electrode, and electrolyte systems. However, although there are a small number of modeling studies, there still exists a significant scarcity of numerical investigations comprehensively analyzing the effects of main parameters on discharge performance.

Given the above situations, an improved one-dimensional mathematical model considering the mass transport, charge conservation, and electrochemical reaction processes for Li-O_2 batteries is developed. Diverging from previous numerical works, the discontinuous deposit of discharge product Li_2O_2 and the formation of by-product Li_2CO_3 due to the electrolyte degradation are simultaneously considered in this model. The effects of primary parameters such as applied current density as well as electrode and electrolyte properties such as porosity and oxygen diffusivity on discharge characteristics are detailedly analyzed employing the model. The results can serve as references and offer a strategic framework for the construction and optimization of efficient Li-O_2 batteries.

2. Theoretical analysis

2.1 Li_2O_2 formation

As schematically depicted in Fig. 2(a), a Li-O_2 battery is composed of a Li metal anode (negative) electrode, an anode protective layer (APL), a microporous separator, and a porous carbon-based cathode filled with an organic electrolyte. Li metal is oxidized in discharging to form Li ions and electrons:

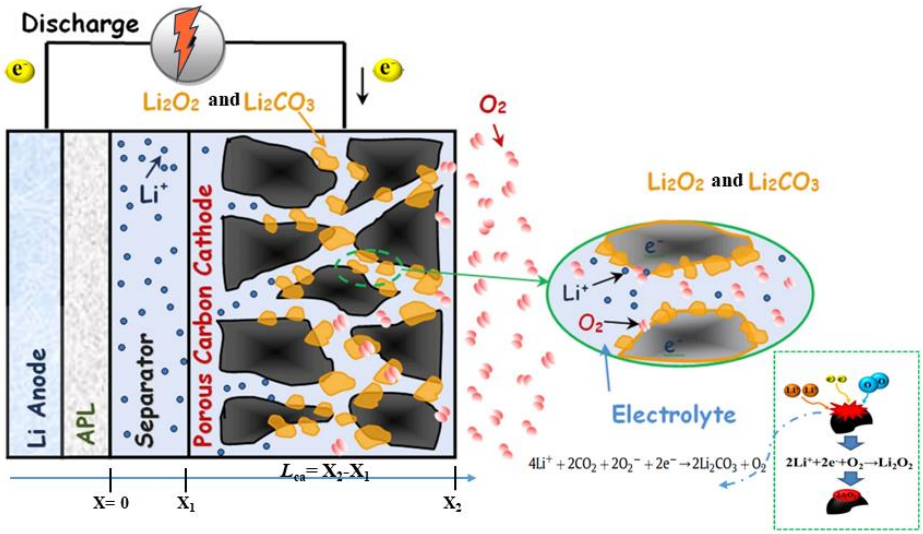
$$\mathrm{Li} \rightarrow \mathrm{Li}^{+} + e^{-} \qquad \text{(I)}$$

They separately transport through the electrolyte and the external circuit to the cathode and react with oxygen to produce Li_2O_2:

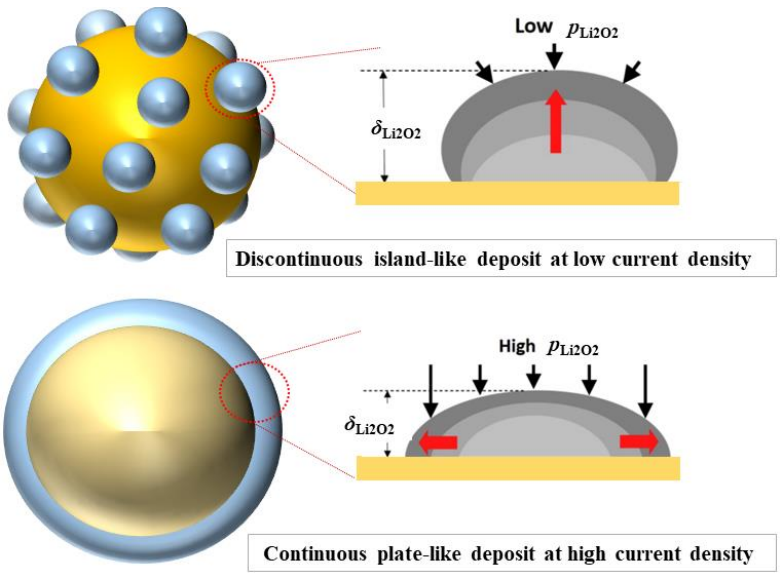
$$2Li^{+} + O_2 + 2e^{-} \rightarrow Li_2O_2 \quad \left(E^0 = 2.96\ \mathrm{V}\right) \qquad \text{(II)}$$

where E^0 denotes the theoretical equilibrium potential for each electrode.

Li_2O_2 is the primary reaction product from oxygen reduction reaction (ORR) due to its insolubility in the organic electrolyte [32,34,36]. It accumulates and forms a layer on the active surface area within the porous cathode, and consequently, the electrochemical reaction and mass transport are hampered, causing the termination of cell discharge. A series of experiments evidenced that a solid film of Li_2O_2 deposits on the carbon surface if the discharge current density is sufficiently large [37]; while at low current density, the surface will preferentially form a discontinuous deposition layer before it is completely covered by the product [38,39], as illustrated in Fig. 2(b).



(a)



(b)

Fig. 2. Schematic of (a) Li-O_2 battery during discharge and (b) the Li_2O_2 formation at low and high discharge current densities.

2.2 Electrolyte degradation and Li_2CO_3 formation

Currently, numerous non-aqueous electrolytes based on various solvents such as ethers, nitriles, carbonates, and ionic liquids, have undergone extensive study and have been implemented in Li-O_2 batteries. Nevertheless, upon discharge from all electrolytes dissolved in various solvents, the by-product Li_2CO_3 generated from electrolyte decomposition was also distinctly identified inside the electrode [6]. Therefore, the electrolyte degradation effect is included in our model.

According to the research of Freunberger et al. [40], Li_2CO_3 formation from the reaction of superoxide reacts with CO_2:

$$2O_2 + 2e^- \xrightarrow{k1a} 2O_2^- \quad (1a)$$

$$2O_2^- + 2CO_2 \xrightarrow{k1b} C_2O_6^{2-} + O_2 \quad (1b)$$

$$C_2O_6^{2-} + 4Li^+ + 2O_2^- \rightarrow 2Li_2CO_3 + 2O_2 \quad (1c)$$

$$\text{Overall} \quad 4Li^+ + 2CO_2 + 2O_2^- + 2e^- \rightarrow 2Li_2CO_3 + O_2 \quad (III)$$

For solvent degradation, it can be elucidated as follows:

$$O_2 + e^- \xrightarrow{k1a} O_2^- \quad (2a)$$

$$2O_2^- + [\text{Solvent}] \rightarrow [\text{Solvent}]^- \quad (2b)$$

$$[\text{Solvent}]^- + O_2 \rightarrow CO_2 + H_2O + 2HCO_2Li + CH_3CO_2Li \quad (2c)$$

$$\text{Overall} \quad 2O_2 + [\text{Solvent}]^- + e^- \rightarrow CO_2 + H_2O + HCO_2Li + CH_3CO_2Li \quad (IV)$$

Indeed, the reaction pathways causing the degradation of the electrolyte and the formation of Li_2CO_3 are complex, involving several intermediate species during battery operation. The above-proposed methods could thus be used to explain the previously known production reaction of Li_2CO_3. For more details regarding the mechanisms, please refer to Refs. [6,40]. Both Li_2O_2 and Li_2CO_3, which are typically insoluble in the electrolyte, can be generated as discharged products when an organic solvent is used as the electrolyte. The repeated deposit of lithium salts hinders species transport and electrochemical reaction and lowers the electronic conductivity of the oxygen electrode

and electrolyte concentration, which results in voltage loss.

3. Mathematical model

3.1. Model assumptions

The present electrochemical-transport-coupled model for non-aqueous Li-O_2 batteries is established by considering key electrochemical reactions and transport phenomena in the sub-regions of a cell. We are particularly interested in examining the impact of various parameters of the porous cathode on Li-O_2 batteries since the porous cathode represents the largest contributor to influence the cell performance considering its greater thickness than both the APL and separator. Also, the following assumptions are made:

(1) The primary discharge products, which only exist and deposit inside the porous cathode, are Li_2O_2 and Li_2CO_3.

(2) To avoid accounting for the thermal effect, the Li-O_2 battery works isothermally.

(3) The non-aqueous electrolyte employed, i.e., 1 M $LiPF_6$ in a 1:2 mixture of propylene carbonate and DME is presumed to be a binary homogeneous monovalent electrolyte.

(4) To model Li+ diffusion, concentrated solution theory is adopted for electrolyte behavior. Also, the mass convection inside the cell is omitted.

(5) The pores within the cathode are filled with liquid electrolyte.

(6) It is assumed that oxygen dissolves in the organic electrolyte with an initially saturated concentration.

3.2. Governing equations

3.2.1. Species transport

The conservation equation of species i (Li^+ and O_2) can be expressed as follows using the porous electrode's macroscopic approach:

$$\frac{\partial\left(\varepsilon C_i\right)}{\partial t} = -\nabla \cdot \boldsymbol{N}_i + S_i \tag{3}$$

where ε is the porosity of the electrode, and it varies with the formation of the solid products, C_i the bulk concentration of species i in the electrolyte, $\boldsymbol{N}_i$ the molar flux of species i in the electrolyte, and S_i the source/sink term due to the electrochemical reaction.

The definition of the Li^+ and O_2 molar flux, when the convection transport is ignored,

is as follows:

$$\boldsymbol{N}_{\mathrm{Li}^+} = -D_{\mathrm{Li}^+,\mathrm{eff}} \nabla C_{\mathrm{Li}^+} + \frac{\boldsymbol{i}_l t_+}{F} \tag{4}$$

$$\boldsymbol{N}_{\mathrm{O}_2} = -D_{\mathrm{O}_2,\mathrm{eff}} \nabla C_{\mathrm{O}_2} \tag{5}$$

where t_+ is the transference number of Li^+, F is Faraday constant (96485 C/mol), $D_{\mathrm{Li+,\,eff}}$ and $D_{\mathrm{O2,\,eff}}$ are the effective diffusivity of Li^+ and O_2, respectively, and can be calculated by the Bruggeman correlation [34]:

$$D_{\mathrm{Li}^+,\mathrm{eff}} = \varepsilon^b D_{\mathrm{Li}^+} \tag{6}$$

$$D_{\mathrm{O}_2,\mathrm{eff}} = \varepsilon^b D_{\mathrm{O}_2} \tag{7}$$

where the Bruggeman factor b of 1.5 is commonly adopted for the Li^+ transport in the non-aqueous electrolytes [35]. $D_{\mathrm{Li+}}$ is defined as a function of Li^+ molar concentration [36]:

$$D_{\mathrm{Li}^+} = \frac{\kappa RT}{z^2 F^2 \left[\mathrm{Li}^+\right]} t_+ \tag{8}$$

where R is the universal gas constant, T is the temperature in Kelvin, z is the charge number of Li^+, and the ionic conductivity is calculated below:

$$\kappa = 0.314 + 1.744 \cdot \left(1 - e^{-0.00135 C_{\mathrm{Li}^+}}\right) \tag{9}$$

The current density in the liquid phase (electrolyte) $\boldsymbol{i}_l$ is determined as:

$$\boldsymbol{i}_l = -\kappa_{\mathrm{eff}} \nabla \phi_l - \frac{2RT\kappa_{\mathrm{eff}}}{F}\left(t_+ - 1\right)\left(1 + \frac{\partial \ln f}{\partial \ln C_{\mathrm{Li}^+}}\right) \nabla \ln C_{\mathrm{Li}^+} \tag{10}$$

where κ_{eff} is the effective ionic conductivity, ϕ_l the potential in the electrolyte, f the activity coefficient of lithium salt.

The current density in the solid matrix phase for the cathode is determined by Ohm's law through the electric potential ϕ_s:

$$\boldsymbol{i}_s = -\sigma_{\mathrm{eff}} \nabla \phi_s \tag{11}$$

Where σ_{eff} denotes the effective electronic conductivity. κ_{eff} and σ_{eff} can be calculated as:

$$\kappa_{\text{eff}} = \varepsilon^{b}\kappa \tag{12}$$

$$\sigma_{\text{eff}} = \left(1-\varepsilon\right)^{b}\sigma \tag{13}$$

where κ and σ are the ionic conductivity of the electrolyte and the electrical conductivity of the electrode.

3.2.2. Conservation of charge

According to the porous electrode theory, the divergence of the total current density must be zero for the solid matrix and solution phases:

$$\nabla \cdot \boldsymbol{i}_{\text{l}} + \nabla \cdot \boldsymbol{i}_{\text{s}} = 0 \tag{14}$$

Also, the transfer current density at the electrode/electrolyte interface at the cathode is obtained by:

$$\nabla \cdot \boldsymbol{i}_{\text{l}} = \sum_{m} a j_{m} \tag{15}$$

where a represents the specific interfacial area and j_{m} denotes the local transfer current density between electrode/electrolyte interface.

Considering both electrochemical reactions of Li_2CO_3 and Li_2O_2 generation inside electrode are included in this study, the production rate of each species (Eq. (2)) from solid phase to pore solution in individual reaction m is given by Faraday's law:

$$S_{\text{i}} = -\sum_{m} \frac{a s_{\text{i,m}}}{nF} j_{m} \tag{16}$$

where $s_{\text{i,m}}$ is the corresponding stoichiometric coefficient of species i.

3.2.3. Electrochemical kinetics

At the Li anode, the local transfer current density (j_{a}) at the electrode/electrolyte interface can be described by:

$$j_{\text{a}} = i_{0}\left[\exp\left(\frac{\left(1-\beta\right)nF}{RT}\eta_{\text{a}}\right) - \exp\left(\frac{-\beta nF}{RT}\eta_{\text{a}}\right)\right] \tag{17}$$

where i_0 is the exchange current density for the cell anode, β is the symmetry factor equal to 0.5, and η_{a} is the overpotential at the anode, which is given by:

$$\eta_{\text{a}} = \phi_{\text{me}} - \phi_{\text{l}} - E_{\text{a}}^{0} \tag{18}$$

where ϕ_{me} and E_a^0 are the potential of metallic lithium and the theoretical equilibrium potential for the lithium dissolution reaction, respectively.

At the cathode of the cell, the Butlere-Volmer equation is adopted to model the kinetics of ORR. For the Li_2O_2 formation, it has:

$$\frac{j_c}{nF} = k_a\left(C_{Li_2O_2}\right)\exp\left[\left(\frac{(1-\beta)nF}{RT}\eta_m\right) - k_c\left(C_{Li^+}\right)^2\left(C_{O_2}\right)\exp\left(\frac{-\beta nF}{RT}\eta_m\right)\right] \quad (19)$$

where k_a and k_c are the reaction kinetics constant of anode and cathode, n is the number of electrons involved, and the cathode overpotential, η_c, is defined as:

$$\eta_c = \phi_s - \phi_l - E^0_{c,m} - \Delta\phi_{Li_2O_2} \quad (20)$$

where $E^0_{c,m}$ and $\Delta\phi_{Li2O2}$ are the theoretical equilibrium potential for each ORR at cathode and voltage loss through the Li_2O_2 deposition layer, and the latter is expressed as [35]:

$$\Delta\phi_{Li_2O_2} = j_c R_{Li_2O_2}\delta_{Li_2O_2} \quad (21)$$

where R_{Li2O2} denotes the electrical resistivity across the Li_2O_2 layer, δ_{Li2O2} is the deposition thickness, and can be evaluated by [35]:

$$\delta_{Li_2O_2} = \frac{d_0\varepsilon_{Li_2O_2}}{2\varepsilon_0} \quad (22)$$

where d_0 represents the distance between two graphene flat, ε_{Li2O2} the volume fraction of Li_2O_2, ε_0 the initial porosity.

CO_2 is formed when the degradation of electrolyte occurs and eventually produces the by-product of Li_2CO_3 during discharge, as analyzed above. First, the superoxide radical anion (O_2^-) forms (Eq.(1a)), and then, it attacks CO_2 that is produced from solvent degradation (Eq.(IV)) to generate Li_2CO_3 with the presence of Li^+, as written below [27]:

$$j_{1a} = Fk_{1a}\left(C_{O_2}\right)\left[-\exp\left(\frac{-\beta nF}{RT}\eta_m\right)\right] \quad (23)$$

$$r_{1b} = k_{1b}\left(C_{O_2^-}\right)\left(C_{CO_2}\right) \quad (24)$$

where k_{1a} and k_{1b} are the reaction rate constants for the formation of O_2^- and Li_2CO_3.

It has been proved the reaction in Eq. (24), which is the rate-determining step (RDS), is first-order concerning both the O_2^- and CO_2 reactants [6,27]. Therefore, other reactions

are regarded as equilibrium, and Eqs. (23) and (24) together can be used to forecast the generation of Li_2CO_3. The kinetics description of CO_2 formation owing to electrolyte degradation is given as follows considering the solvent concentration in Eq. (IV):

$$j_{\mathrm{IV}} = Fk_{\mathrm{IV}}\left(C_{\mathrm{O_2}}\right)\left[-\exp\left(\frac{-\beta nF}{RT}\eta_{\mathrm{m}}\right)\right] \tag{25}$$

where k_{IV} is the reaction rate constant for the formation of CO_2.

3.2.4. Transport through the Li_2O_2 deposition and porosity change

Li_2O_2 deposits increasingly onto carbon surfaces as discharge depth increases or state of charge (SOC) decreases, reducing the effective surface area and impeding the supply of Li^+ and O_2. Consequently, the surface coverage of Li_2O_2 onto carbon surfaces, θ, which represents a fraction of the adsorption sites occupied by Li_2O_2, is a significant factor in determining the comprehensive discharge performance. It can be computed by the following empirical formula [36]:

$$\theta = \mu\left(\frac{\varepsilon_{\mathrm{Li_2O_2}}}{\varepsilon_0}\right)^{\gamma} \tag{26}$$

where the geometric factors of μ and γ signify the effects of the substrate and deposit morphology. The former describes the influence of partial pressure of the adsorption species, which is largely owing to the geometrical shape of the substrate. If the substrate, i.e., carbon-based material at the cathode, is viewed as a rigorous sphere, μ equals 1. Apparently, for a specific μ, Eq. (26) can be utilized to investigate the impact of γ on the surface coverage of Li_2O_2.

As depicted in Fig. 2(b), a small Li_2O_2 pressure resulting from the low current density causes fewer nucleation sites, which leads to the formation of island-like deposits on carbon surfaces. Thus, γ possesses a large value approaching 1 in this circumstance. Contrarily, γ has a small value that approaches 0 at very high discharge current densities due to the production of plate-like deposits that occupy plenty of nucleation sites [36]. Hence, γ can be described as inversely proportional to discharge current density:

$$\gamma = \frac{C}{\boldsymbol{i}_{\mathrm{m,app}}} \tag{27}$$

where $\boldsymbol{i}_{\mathrm{m,app}}$ denotes the mass-specific current density which is defined below:

$$\boldsymbol{i}_{\mathrm{m,app}} = \frac{\boldsymbol{i}_{\mathrm{app}}}{M \cdot h_{\mathrm{c}}} \tag{28}$$

where $\boldsymbol{i}_{\mathrm{app}}$ and M are the applied current density and mass loading of carbon per unit volume of cell cathode. h_{c} is an empirical constant, which is primarily influenced by materials utilized for electrolytes and catalysts. In this study, the value of 1.68 mA/g is adopted by fitting the experimental data. Also, the deposits of products are regarded to be distributed uniformly.

Fick's law is used to calculate the diffusion flux for the transfer of Li^+ and O_2 through the deposition layer:

$$C_{\mathrm{Li_2O_2}} = C_{\mathrm{i}} + \frac{\delta_{\mathrm{Li_2O_2}} j_{\mathrm{c}}}{D_{\mathrm{i,Li_2O_2}} \cdot nF} \tag{29}$$

where the effective diffusion coefficients of species and other parameters are analyzed before, the thickness of the deposition layer, δ_{DL}, is obtained by:

$$\delta_{\mathrm{DL}} = \left(\sqrt[3]{\frac{\varepsilon_{\mathrm{DL}}}{1-\varepsilon}} + 1 \right) r_{\mathrm{cb}} \tag{30}$$

where $\varepsilon_{\mathrm{DL}}$ and r_{cb} represent the volume fraction of the deposited layer and the radius of carbon-based material used for the cathode, and the former is estimated by:

$$\varepsilon_{\mathrm{DL}} = \frac{\varepsilon_{\mathrm{Li_2O_2}}}{\theta} \tag{31}$$

The specific area of the electrode/electrolyte interface is reduced because of Li_2O_2 and Li_2CO_3 coverage, and the variation of effective surface area per unit volume is approximated by a geometric relation as [41]:

$$a = a_0 \left[1 - \left(\frac{\varepsilon_{\mathrm{s}}}{\varepsilon_0} \right)^p \right] \left[1 - \frac{\delta_{\mathrm{s}}}{\delta_{\mathrm{max}}} \right] \tag{32}$$

where a_0 and ε_{s} denote the initial specific surface area of electrode porosity and the volume fraction of solid discharge products, δ_{s} and δ_{max} are the thickness of products and the maximum thickness of products film to allow charge transport, which is 10 nm. p is a geometrical factor implying the morphology of the solid product that covers the active area, the value of 0.4 is used in this model.

The solid depositions generated during discharge cover the surface and fill the void space in the porous cathode, the volume change because of the accumulation of Li_2O_2 and Li_2CO_3 is expressed as:

$$\frac{\partial \varepsilon}{\partial t} = \sum_{\text{solid phase } m} aj_m \frac{M_{\text{m}}}{nF\rho_{\text{m}}} \tag{33}$$

where M_{m} and ρ_{m} signify the molar mass and density of solid discharge products.

3.3. Initial and boundary conditions

Each species' concentration is expected to be equal to its starting concentration and to be distributed uniformly across the cell system. The porous cathode is regarded as the key portion of the computational domain affecting battery performance as its thickness is significantly greater than that of the APL and separator.

From Fig. 1(a), at the APL/separator interface (x=0), lithium metal is electro-oxidized to offset the loss of Li^+ and electric migration in the electrolyte:

$$-\frac{\partial \boldsymbol{N}_{\text{Li}^+}}{\partial x} = \left(1+t_+\right)\frac{\boldsymbol{i}_{\text{app}}}{F} \tag{34}$$

At the separator/cathode interface (x= x1, boundary 1)

$$\boldsymbol{i}_{\text{s}} = -\frac{\partial \phi_{\text{s}}}{\partial x} = 0;\ \boldsymbol{i}_{\text{l}} = \boldsymbol{i}_{\text{app}};\ \boldsymbol{N}_{\text{O}_2} = 0;\ \boldsymbol{N}_{\text{Li}_2\text{O}_2} = 0; \tag{35}$$

At the cathode/current collector interface (x= x2, boundary 2)

$$\boldsymbol{i}_{\text{s}} = \boldsymbol{i}_{\text{app}};\ \boldsymbol{i}_{\text{l}} = 0;\ \boldsymbol{N}_{\text{Li}^+} = 0;\ C_{\text{O}_2} = S_{\text{O}_2};\ \boldsymbol{N}_{\text{Li}_2\text{O}_2} = 0 \tag{36}$$

where S_{O2} denotes the O_2 solubility in the electrolyte.

Additionally, the cell voltage is determined using the difference between the electrolyte potential on the anode side and the electrode potential at the cathode current collector, as written below:

$$E = \phi_{\text{s}}\left(x = x2\right) - \phi_0\left(x = 0\right) \tag{37}$$

3.4. Numerical implementation and model validation

The governing equations coupling charge conservation, species transport, and reaction kinetics, together with the boundary conditions in this model, are resolved using a finite element method with time-dependent. Partial differential equations (PDEs) and

related variables that are programmed within the software tool utilizing user-defined functions are discretized by the non-linearity Newton method. The time-dependent solver adopted is MUMPS. Also, the backward differentiation formula (BDF) scheme is chosen as a time stepper, and the iterative approach adopted by the solver is the generalized minimal residual method (GMRM) [42]. The self-adaptive step is used during calculation and when the relative tolerance is lower than 10^{-4}, the solution is regarded as having converged. The main parameters used for numerical computation are listed in Table 1.

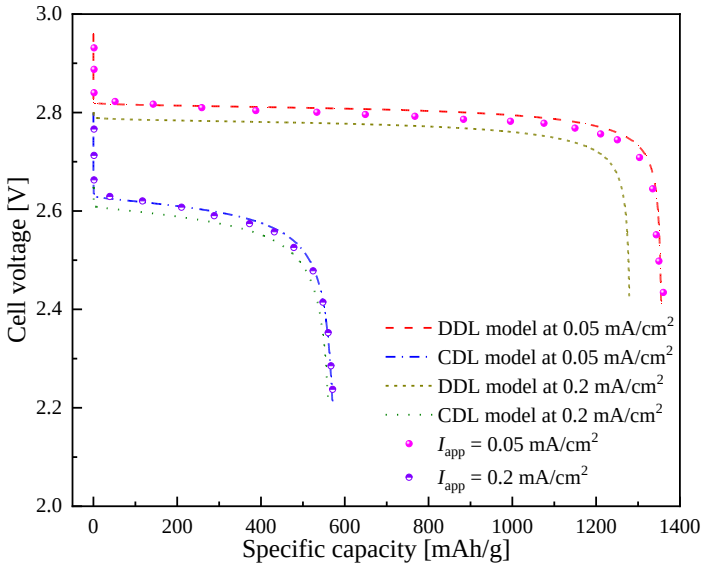


Fig. 3. Comparisons between simulated discharging curves and experimental data [43].

To examine the correctness of the simulation approaches employed in this paper, the discharge behaviors at different current densities between the simulation in this work and the experiment performed by Read et al. [43] are compared. Two numerical models are separately used: the discontinuous deposit layer (DDL) of discharge product model (Fig. 2(a)) and the general continuous deposit layer (CDL) of discharge product model (Fig. 2(b)). It can be seen from Fig. 3 that although both models can predict the discharge behavior, the results obtained using the DDL model are closer to the experimental data, especially for the case with low current density (I_{app} = 0.05 mA/cm^2), which conforms to the abovementioned theoretical analysis. The experimental results show that the battery voltage almost remains constant at 0.05 mA/cm^2, followed by a fast drop to the cut-off voltage. At a higher current density of 0.2 mA/cm^2, the voltage linearly decreases and then quickly drops. Generally, Li-O_2 batteries operate at a discharge current density below 0.4 mA/cm^2 [36].

Table 1. Parameters used for numerical simulations [32,34–36,41].

Parameters	Value	Unit	Symbol
Thickness of separator	$5\cdot10^{-5}$	m	L_{se}
Thickness of cathode electrode	$7.5\cdot10^{-5}$	m	L_{ca}
Porosity of the cathode	0.73	–	ε_0
Conductivity of cathode electrode	100	S/m	σ
Porosity of the cathode	0.73	–	ε_0
Specific surface area of cathode	$3.67\cdot10^{7}$	m^2/m^3	a
Electrical resistivity across Li_2O_2 film	50	$\Omega\cdot m^2$	R_{Li2O2}
Electrolyte concentration	1000	mol/m^3	C_{Li+}
External oxygen concentration at 1 atm	9.46	mol/m^3	$C_{O2,ext}$
Solubility factor of oxygen	0.38	–	S_{O2}
Solubility limit of Li_2O_2 dissolved in electrolyte	0.09	mol/m^3	C_{max}
O_2 diffusion coefficient	$7\cdot10^{-10}$	m^2/s	D_{O2}
Transference number of Li^+	0.26	–	t_+
$\partial\ln f/(\partial\ln C_{Li})$	–1.03	–	–
Reaction rate coefficient anodic current	$1.11\cdot10^{-15}$	m/s	k_a
Reaction rate coefficient cathodic current	$3.4\cdot10^{-17}$	$m^7/s/mol^2$	k_c
Reaction rate coefficient for O_2^- formation	$8\cdot10^{-15}$	m/s	k_{1a}
Reaction rate coefficient for Li_2CO_3 formation	350	$m^3/s/mol^2$	k_{1b}
Reaction rate constant of CO_2 formation	$5.9\cdot10^{-15}$	m/s	k_{IV}
Exchange current density for anode	1	A/m^2	i_0
Dissolution rate coefficient of Li_2O_2	4	1/s	k_d
Symmetry factor	0.5	–	β
Mass density of Li_2O_2	2140	kg/m^3	ρ_{LiO2}
Mass density of Li_2CO_3	2110	kg/m^3	ρ_{Li2CO3}
Mass density of electrolyte solution	1200	kg/m^3	ρ_{LiPF6}
Mass density of carbon	2260	kg/m^3	ρ_C
Particle radius in the electrode	$25\cdot10^{-9}$	m	r_0
Operating temperature	300	K	T
Standard potential of the ORR	2.96	V	Φ_{ORR}

4 Results and discussion

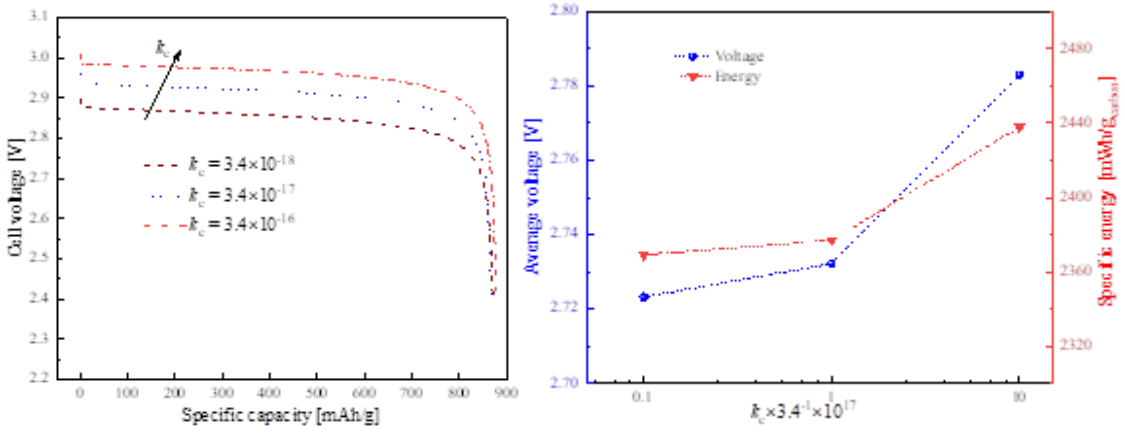
4.1. Cathode design

The cathode plays a critical role in the discharge characteristics of Li-O_2 batteries. In this section, the effect of reaction catalytic activity, cathode geometry, and initial porosity

of the cathode on discharge performance are numerically studied and discussed.

4.1.1. Effect of reaction activity

One possibility is that the used catalysts, such as metal oxide catalysts and noble metal catalysts with carbon active materials, can minimize the overpotential and hence boost the efficiency of the cell since the performance of the cell depends on the porous electrode. The influence of cathodic rate constant (k_c) on the discharge voltage of the cell as a function of specific capacity is portrayed in Fig. 4(a) to study the impact of various catalysts on battery behavior. Inside the cathode, this rate coefficient is presumptively constant and distributed uniformly. As can be seen, the discharge voltage plateau exhibits an ascendent trend with the larger k_c because of the decreased overpotential of the cathode electrode. On the other hand, the specific capacity almost remains the same. When augmenting k_c from the base value (3.4×10^{-17}) to 3.4×10^{-16}, the average discharge voltage is heightened from 2.73 V to 2.78 V, as depicted in Fig. 4(b), and the obtained voltage plateau after magnifying is around 2.96 V, which is consistent with the theoretical equilibrium voltage for Li_2O_2 formation. Additionally, the specific energy is slightly elevated from 2369 mWh/$g_{\text{-carbon}}$ to 2438 mWh/$g_{\text{-carbon}}$ when increasing k_c from 3.4×10^{-18} to 3.4×10^{-16}. The results prove that the enhanced k_c can not only strengthen the ORR inside the cell cathode but also improve the discharge voltage and energy density.



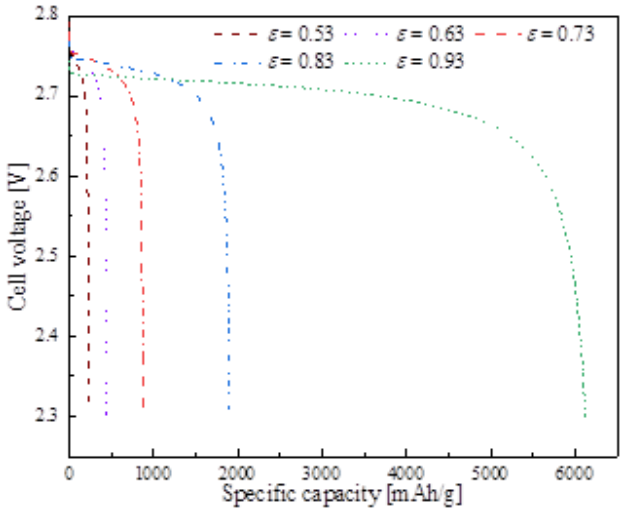
(a) (b)

Fig. 4. Effect of k_c on (a) voltage-capacity curve and (b) energy density.

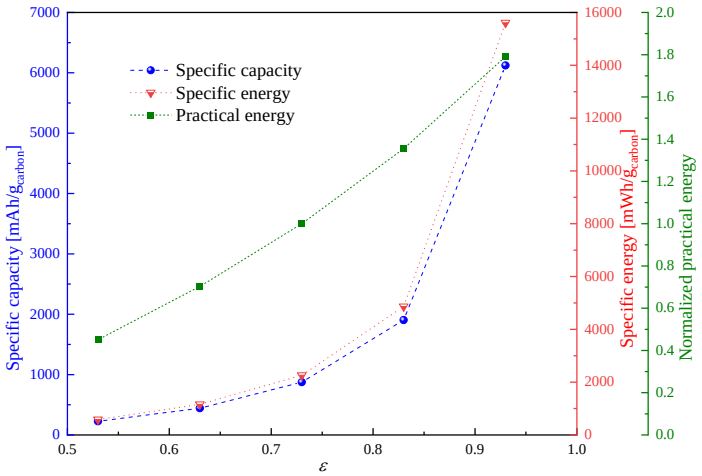
4.1.2. Effect of initial porosity

The findings demonstrate that the battery capacity rises when more room is made available to accommodate discharge products for the situation of changing initial cathode porosity ε, and the voltage plateau is also slightly improved, as elucidated in Fig. 5(a). With

the increase of ε from 0.53 to 0.93, the specific capacity is enlarged from 226 mAh/$g_{\text{-carbon}}$ to 6122 mAh/$g_{\text{-carbon}}$, and the corresponding specific energy upgrades from 585.5 to 15610 mWh/$g_{\text{-carbon}}$, as presented in Fig. 5(b).



(a)

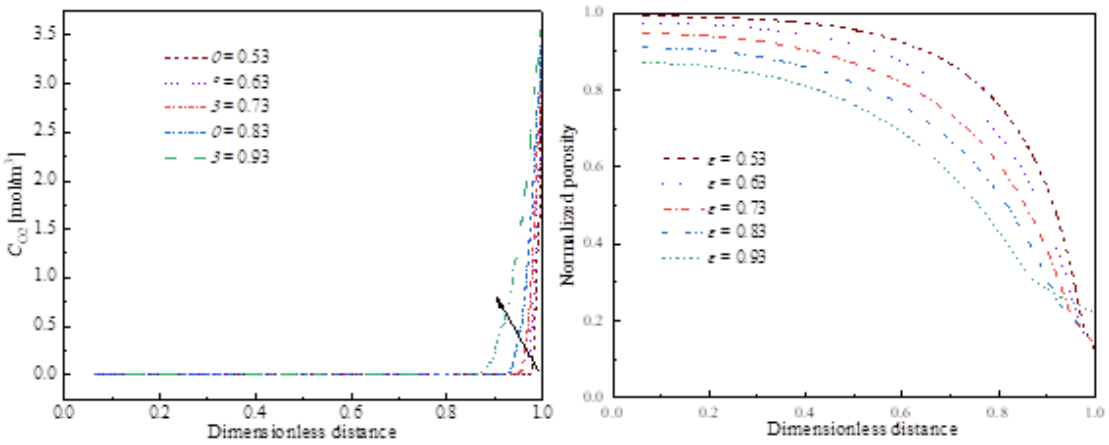


(b)

Fig. 5. Effect of ε on (a) voltage-capacity curve and (b) energy density.

Furthermore, it can be observed that the amplification of capacity prominently increases as the rise step of ε is fixed at 0.1. Parameterization of energy densities obtained for various other porosity cases using the base case (ε =0.73) as a reference, Fig. 5(b) also discloses that even considering the normalized practical energy, it still rises as the porosity increases. This is due to the limited void space to accommodate the solid product of Li_2O_2 and the high transportation resistance at low porosity. When elevating the porosity from the reference value of 0.73 to 0.93, the practical total energy realizes an ascent of approximately 80%. The results highlight the importance of abundant pores in the construction of cathode materials for Li-O_2 batteries.

The C_{O2} profiles along dimensionless distance at the end of discharge under different initial cathode porosity are exhibited in Fig. 6(a). As can be seen, the C_{O2} within the cell cathode with a low initial porosity is lower than that with a greater porosity at the same distance. This can be ascribed to the low utilization of the pore volume at the end of discharge, which leaves open spaces for oxygen diffusion, as shown in Fig. 6(b). The porosity distribution of cathode at the end of discharge is more uniform for the case with high initial ε because large ε can not only promote the species transport but also provide more sites to accommodate the solid products. Therefore, a large porosity is essential for species transportation and solid product buildup in order to achieve a high discharge specific capacity.



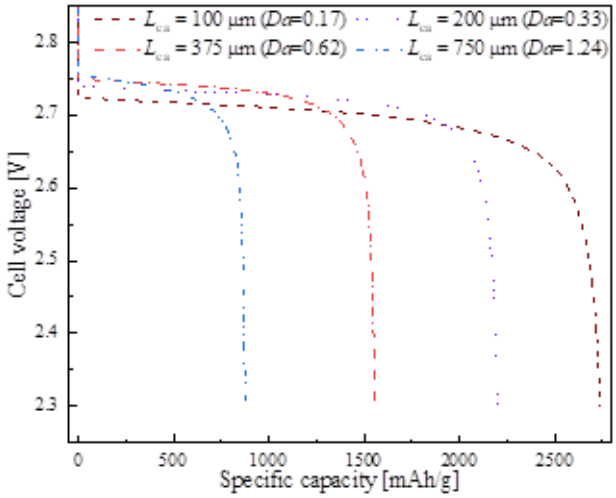
(a) (b)

Fig. 6. Effect of initial porosity on (a) C_{O2} and (b) normalized ε.

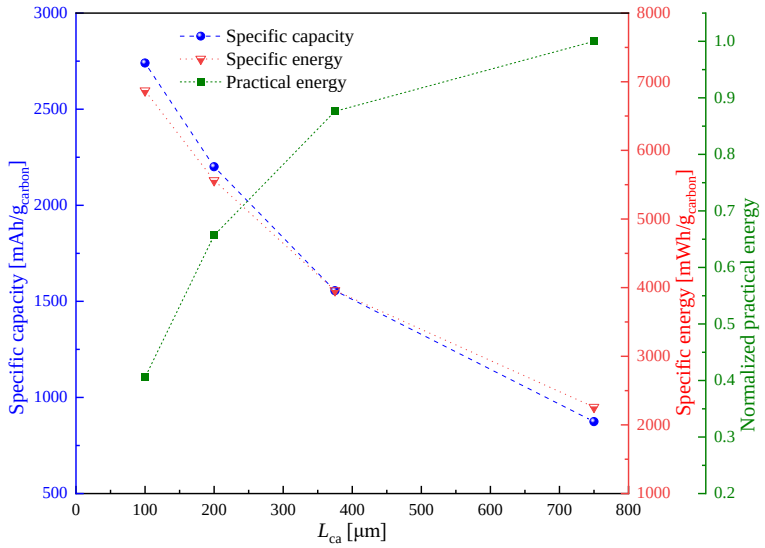
4.1.3. Effect of cathode thickness

The cathode thickness is momentous in determining how Li_2O_2 deposits affect the cathode usage and effective surface area, ultimately controlling the discharging performance. As the cathode thickness is reduced, the mass loading of carbon diminishes, increasing the discharge current density per mass of carbon. As a result, using various cathode thicknesses, it is possible to alter the surface coverage of Li_2O_2 deposits on carbon surfaces. Additionally, the transportation resistance of species, which is proportional to cathode thickness, might have a noticeable impact on the cathode utilization. To analyze the influence of cathode thickness, the dimensionless Damköhler number *Da*, which characterizes the electrochemical reaction rate to oxygen diffusion rate, is introduced as:

$$Da = \frac{j/nF}{D_{O_2,\mathrm{eff}} \cdot C_{O_2}/L} \tag{38}$$



(a)



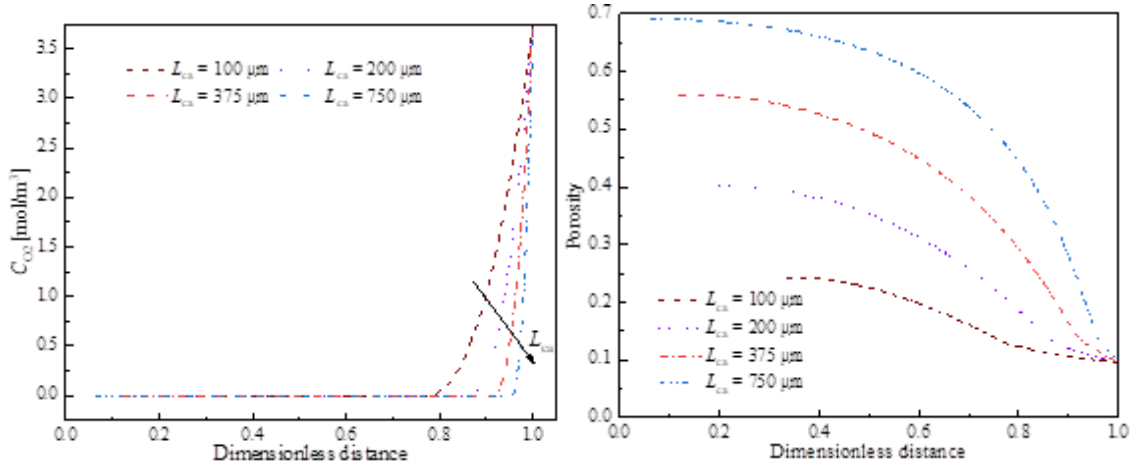
(b)

Fig. 7. Effect of L_{ca} on (a) voltage-capacity curve and (b) energy density.

Apparently, a unity of *Da* signifies an equal rate of surface electrochemical reaction and O_2 mass transfer owing to diffusion. As unveiled in Fig. 7(a), although the cell discharge voltage slightly drops because of a reduction in the effective surface area, the specific capacity boosts as the cathode thickness is shortened (*Da* is decreased). When *Da* is relatively large (more than 1), the cell performance is restricted by the O_2 diffusion which possesses a low diffusion coefficient in non-aqueous electrolytes. Therefore, Li-O_2 batteries yield a small specific capacity for the thicker electrode and a great value for the thinner electrode. Fig. 7(b) manifests that when lengthening L_{ca} from 100 μm to 750 μm, the specific capacity descends from 2740.3 to 874.4 mAh/$g_{\text{-carbon}}$, and the corresponding specific energy declines from 6868.6 to 2258.2 mWh/$g_{\text{-carbon}}$, dropping 67.1%. Hence, a thin cathode is conducive to the specific capacity. On the other hand, a thinner layer of

cathode means that the active material is loaded less, which could result in a smaller practical capacity. From Fig. 7(b), the practical energy discounts 59.4% as L_{ca} reduces from the base case (750 μm) to 100 μm.

The profiles of C_{O2} and ε along dimensionless distance at the end of discharge under various cathode lengths (or thicknesses) are drawn in Fig. 8. As observed, the dimensionless depth for O_2 penetration diminishes with rising thickness (Fig. 8(a)), meaning a high O_2 transport barrier. Consequently, the utilization of the porous cathode lessens with thickness, as proved in Fig. 8(b). This is because, for the thicker cathode, Li-O_2 batteries will be subject to the oxygen diffusion-controlled limitation. To overcome this challenge, the electrolyte with high solubility and diffusivity of oxygen which can decrease the *Da* number is preferred. Overall, careful design and arrangement of the cathode thickness are indispensable with considering the trade-off between the specific energy/capacity and the practical capacity.



(a) (b)

Fig. 8. Effect of L_{ca} on (a) C_{O2} and (b) ε.

4.2. Effect of Li-O_2 batteries operating condition

Since in reality, batteries undergo charging and discharging processes under different operating conditions, this section will simulate the discharging behaviors and performance of Li-O_2 batteries under various operating conditions.

4.2.1. Effect of applied current density

Discharge current density is one of the critical indicators that can affect the formation of discharge product deposition. Fig. 9 presents the discharge behaviors of Li-O_2 batteries at the current density of 0.05, 0.1, 0.2, and 0.5 mA/cm^2. One can see that low I_{app}

contributes to the specific capacity, the value increases from 269.9 mAh/$g_{\text{-carbon}}$ to 1354.9 mAh/$g_{\text{-carbon}}$ when I_{app} is enlarged from 0.05 mA/cm^2 to 0.5 mA/cm^2, which is consistent with experiment results [43]. Besides, the voltage plateau is inversely proportional to discharge current density, e.g., the voltage plateaus are around 2.6 V and 2.81 V for the cases of 0.1 mA/cm^2 and 0.5 mA/cm^2. The results emphasize that the I_{app} of Li-O_2 batteries should be as low as possible under the condition of meeting the application requirement.

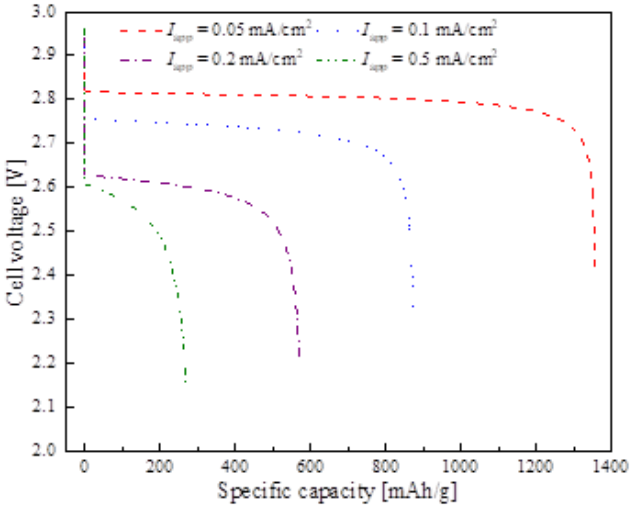
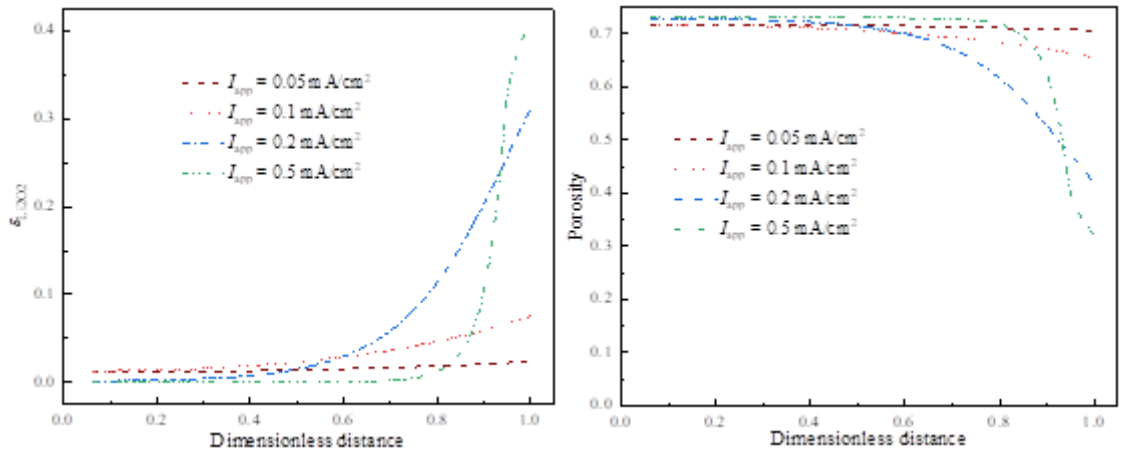


Fig. 9. Discharge curves at different current densities.

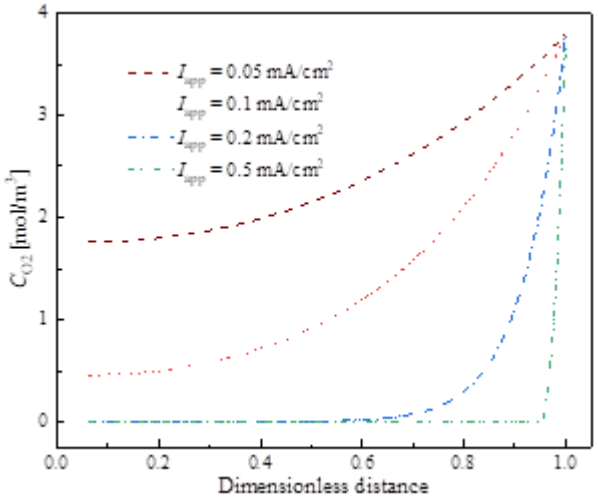
Three important characteristics of Li-O_2 batteries cathode during discharging: Li_2O_2 volume fraction ε_{Li2O2}, porosity ε, and oxygen concentration C_{O2}, are predicted to reveal the discharge behavior of batteries. At a given time, the changes of the abovementioned characteristics along the cathode thickness at various current densities are plotted in Fig. 10. As observed in Fig. 10(a), Li_2O_2 deposition builds up near the cathode current collector where the O_2 concentration is high, the ε_{Li2O2} is approximately 2.37%, 7.52%, 31.04%, and 40.74% respectively at cathode/current collector interface, which is significantly higher than that of separator/cathode interface because of low O_2 transport. For the cases using large current densities, ε_{Li2O2} dramatically accumulates near the cathode/current collector interface, consequently, the porosity of cathode rapidly reduces, which is also demonstrated in Fig. 10(b). In other words, a higher I_{app} will cause a fast accumulation of discharge products and a rapid decrease of porosity at the cathode, and subsequently terminate the cell discharge. Specifically, at 0.5 mA/cm^2, the ε at boundary 2 is 49.27% of the case using 0.1 mA/cm^2.

Fig. 10(c) suggests that at the same position, C_{O2} is lower for the cases with large I_{app}, which can be attributed to the low O_2 transport capability. The reason is a faster

electrochemical reaction due to the high I_{app} results in prompt O_2 consumption. At 0.2 and 0.5 mA/cm^2, C_{O2} is almost zero in most areas and the electrochemical reaction does not proceed sufficiently, indicating that many areas of the cathode are not effectively utilized at this moment.



(a) (b)



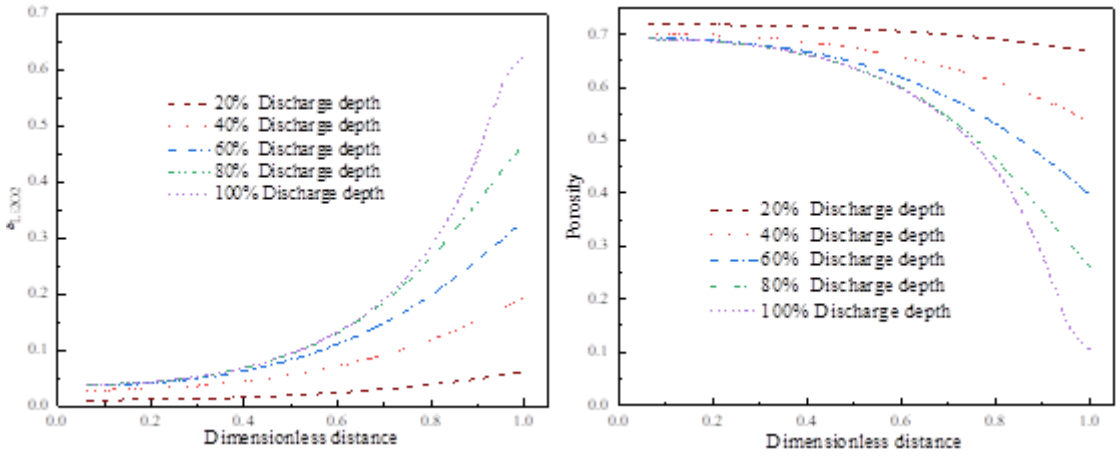
(c)

Fig. 10. Effect of I_{app} on (a) ε_{Li2O2}, (b) ε, and (c) C_{O2}.

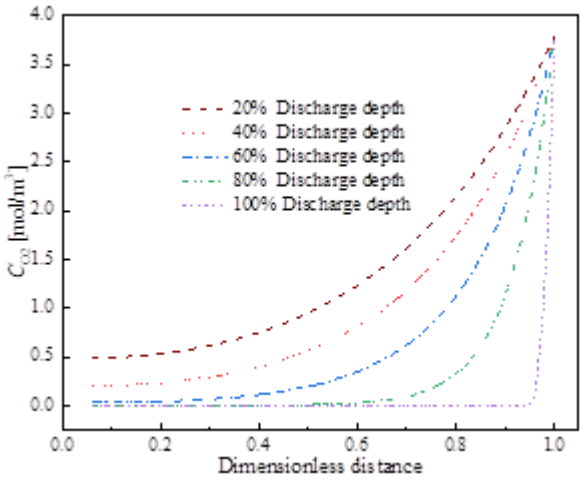
4.2.2. Effect of discharge depth

To investigate the effect of some key parameters on Li-O_2 batteries, a current of 0.1 mA/cm^2 is used in this and subsequent parts. Fig. 11(a) presents the ε_{Li2O2} profiles inside the Li-O_2 batteries during discharging at various discharge states. As the state of discharge (SOD) increases, ε_{Li2O2} has the propensity of ascendent, especially for the position close to the cathode/current collector interface. This is because Li_2O_2 is continuously generated at the porous cathode of the cell, and the gradual growth of it on the active surface reduces the available pores for electrolyte resulting in Li_2O_2 insulated film and pore blockage, as

depicted in Fig. 11(b). Taking SOD of 20% as an example, the ε_{Li2O2} and ε at boundary 2 are 6.19% and 66.81%, respectively, while at 80% SOD, the corresponding values are 46.84% and 26.16%. Both Li_2O_2 deposits and pore blockage cause restriction of O_2 transfer (Fig. 11(c)) and severely limit the battery capacity. To surmount this issue, the appropriate carbon material that has a sufficient amount of pores spread across the entire electrochemically active surface should be developed as a cathode to accommodate the discharge products.

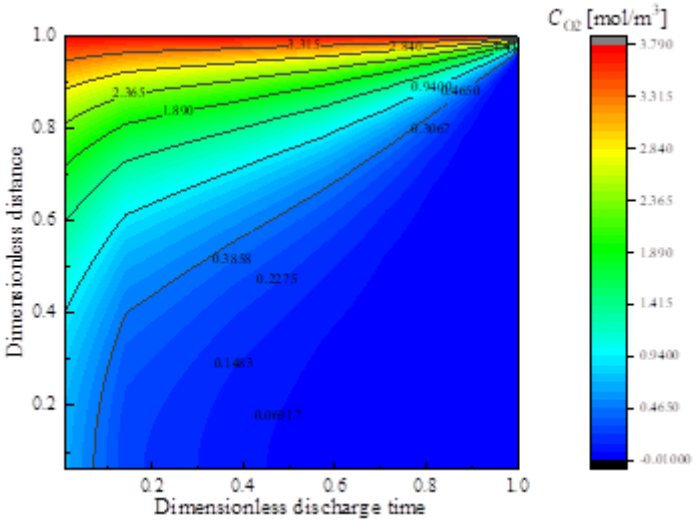


(a) (b)

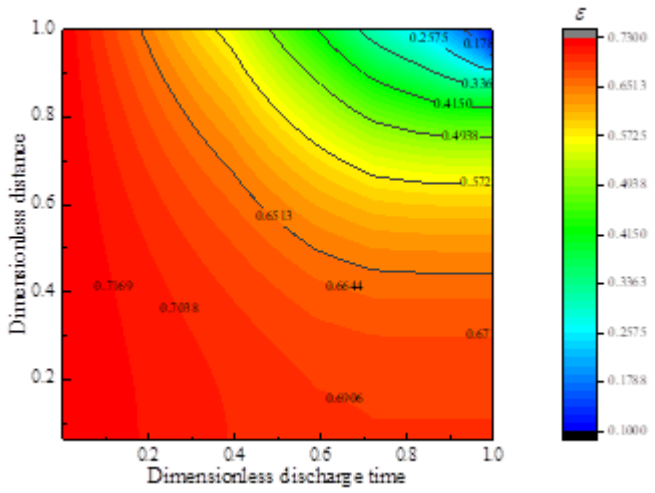


(c)

Fig. 11. Effect of discharge depth on (a) ε_{Li2O2}, (b) ε, and (c) C_{O2}.



(a)



(b)

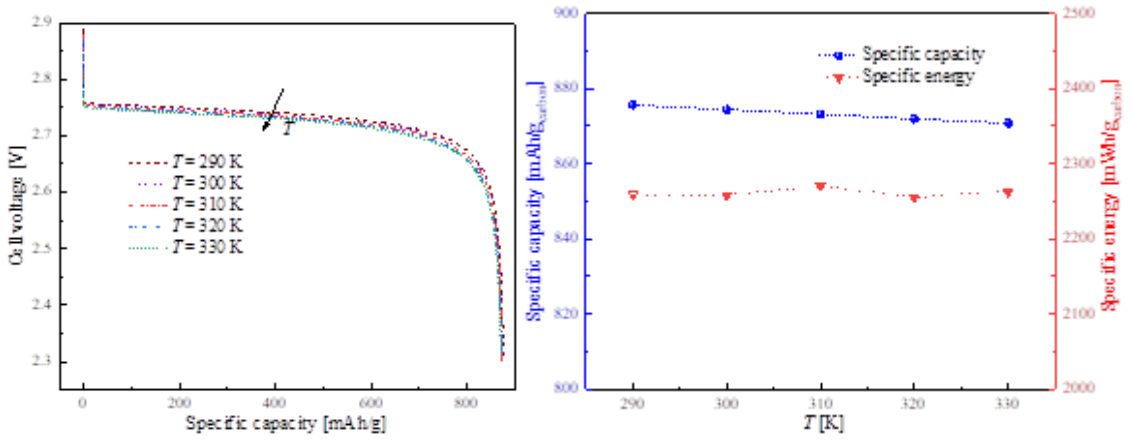
Fig. 12. Variations of (a) C_{O2} and (b) ε with dimensionless distance and dimensionless discharge time.

The overall profiles of C_{O2} and ε with dimensionless distance and dimensionless discharge time are illustrated in Fig. 12(a) and (b). The contour lines in Fig. 12(a) indicate that the C_{O2} at the cell cathode declines with discharge time whereas rises along the thickness direction. Namely, the maximum value appears in the upper left position of the cloud image, that is, the solubility of O_2; the minimum value appears in the lower right corner, close to 0. From Fig. 12(b), the minimum ε appears in the upper right corner while the maximum value locates in the lower left corner. The reason is, as explained above, with the advancement of the discharge process, the porosity of the same position of the battery cathode gradually decreases due to the deposition of Li_2O_2 and pore blockage; in addition, the electrochemical reaction mainly occurs near the cathode/current collector interface (dimensionless distance equals 1), while the reaction hardly occurs at the

separator/cathode interface (dimensionless distance equals 0).

4.2.3. Effect of working temperature

Temperature is one of the key thermodynamic parameters that should be considered for cells. Fig. 13(a) shows that the effect of regular operating temperature on the discharge behavior is insignificant. When boosting the temperature from 290 K to 330 K, the discharge plateau tends to descend but the specific capacity of the cell is almost the same, i.e., ~870 mAh/g (under the condition of I_{app} =0.1 mA/cm^2). Even so, the difference in the discharge plateaus at the above temperature range is small, and the corresponding values are around 2.73 V. Fig. 13(b) further verifies that the effect of working temperature on cell energy density is small. The ESD range is 2258.2-2270.8 mWh/$g_{\text{-carbon}}$ at the selected temperature range.



(a) (b)

Fig. 13. Effect of T on (a) voltage-capacity curve and (b) energy density.

Although the simulated results manifest that the discharge behavior of Li-O_2 batteries is not very sensitive to regular operating temperature, it is still necessary to avoid the battery working at an excessive temperature to prevent the discharge voltage not reaching the actual demand and the occurrence of thermal runaway. Please note that temperature only affects the electrochemical reaction kinetics in the present model. In reality, however, many parameters are affected by temperature to varying degrees. For example, the species diffusivity, the conductivity of an electrolyte, and the oxygen solubility are all functions of temperature, making the effect of temperature on the operation of Li-O_2 batteries more complex. Due to the lack of specific functional relationships between these parameters and temperature, some parameters are set to reasonable constant values in this model. In future work, it is pivotal to establish the relationship between the relevant parameters and

temperature, so as to numerically reveal the charging/discharging characteristics of the battery at different temperatures more accurately.

4.3. Electrolyte regulation

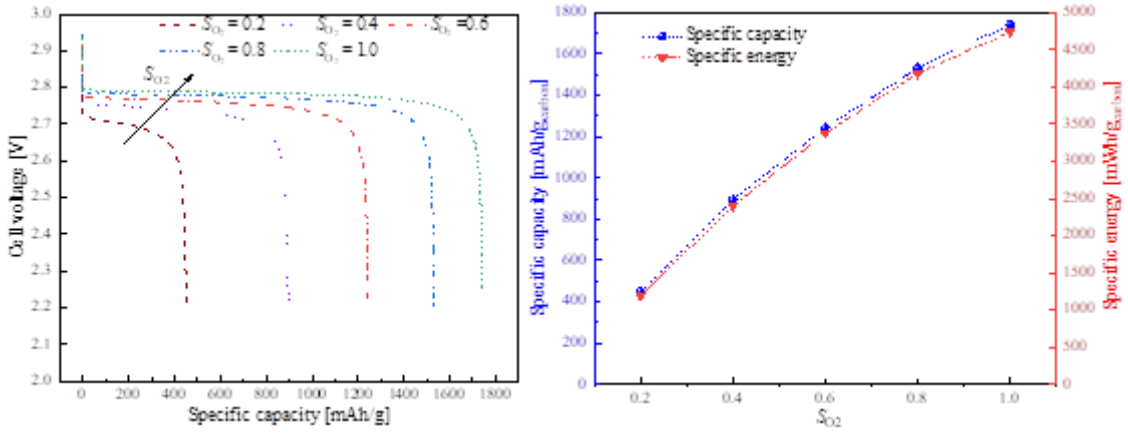
High ionic conductivity, high oxygen solubility and diffusivity, and strong chemical and electrochemical stability, are all desirable properties for a non-aqueous electrolyte used in Li-O_2 batteries. In this part, the effects of transport properties on discharge performance will be explored. The above characteristics are assumed to be independent so that their impact on the ESD and discharge capacity can be compared and assessed.

4.3.1. Effect of oxygen solubility

To investigate the impact of oxygen solubility S on the discharge characteristics, S_{O2} is changed from 0.2 to 1.0 with a step of 0.2, and the cut-off voltage is set at 2.2 V. Fig. 14(a) suggests that both the discharge voltage and specific capacity increase with S_{O2}. When enhancing S_{O2} from 0.2 to 1, the voltage plateau rises from 2.68 V to 2.77 V, and the capacity extends from 449.9 mAh/$g_{\text{-carbon}}$ to 1532.1 mAh/$g_{\text{-carbon}}$ (an increase of 240.5%). The amelioration in discharge voltage comes from the intensified reaction kinetics thanks to the increased O_2 concentration in the electrolyte, as implied in Eq. (19), which in turn generates more Li_2O_2 and brings a greater capacity. When further elevates S_{O2} from 0.8 to 1, the amplification in discharge plateau and capacity are not as significant as before, which are 2.79 V and 1742.5 mAh/$g_{\text{-carbon}}$, although they still keep an increasing trend, as displayed in Fig. 14(b). This can be ascribed to the limited pore volume of the cell cathode for solid product accumulation. Fig. 14(b) also provides the specific energy densities of the cell under different S_{O2}. The energy density exhibits a similar growth trend to capacity because the difference in discharge voltages is relatively small. The specific energy surges to 4742.4 mW/$g_{\text{-carbon}}$ from 1192.2 mW/$g_{\text{-carbon}}$ when S_{O2} rises from 0.2 to 1.0, realizing a 297.8% lift.

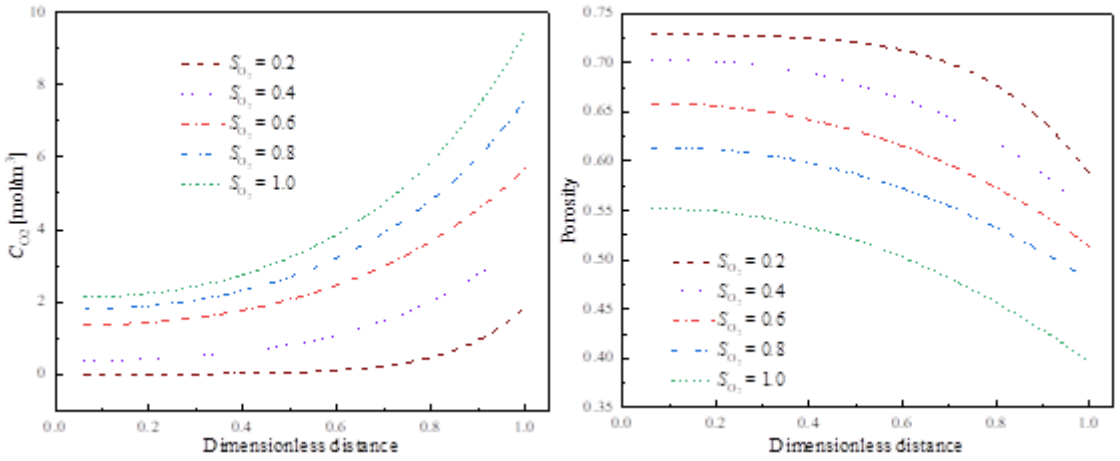
The C_{O2} and ε profiles under different oxygen solubility S_{O2} at a fixed SOD are depicted in Fig. 15. As can be seen, the C_{O2} at the same position of the cell cathode is greater for the case with higher S_{O2} (Fig. 15(a)). Despite this, the C_{O2} still increases with the dimensionless distance, this non-uniform electrochemical reaction at the cathode can be attributed to the restricted O_2 transportation. Fig. 15(b) demonstrates the inference that high C_{O2} promotes the electrochemical reaction and subsequently leads to considerable products, as a result, ε decreases with the increasing S_{O2} at this given SOD. For instance,

when the dimensionless distance is 0.6, the values of ε are 0.713 and 0.502 for the cases of S_{O2}=0.2 and S_{O2}=1. Consistent with the previous analyses, the reaction near boundary 2 is more rapid due to the higher O_2 concentration, so that ε of the cathode shows a gradual decline along the thickness direction.



(a) (b)

Fig. 14. Effect of oxygen solubility on (a) voltage-capacity curve and (b) energy density.



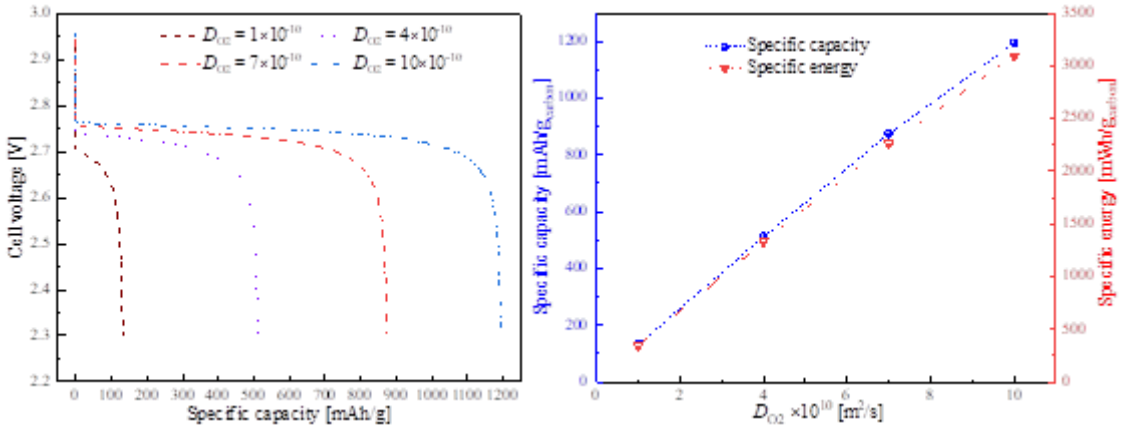
(a) (b)

Fig. 15. Effect of oxygen solubility on(a) C_{O2} and (b) ε.

4.3.2. Effect of oxygen diffusivity

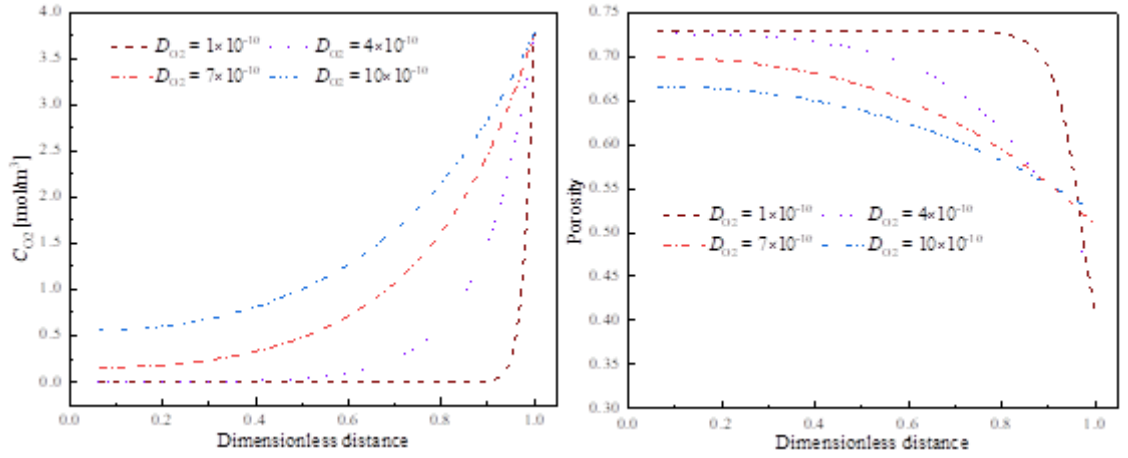
To investigate the influence of oxygen diffusivity D_{O2} on the cell discharge performance, similarly, the range of D_{O2} from 1×10^{-10} to 10×10^{-10} m^2/s is adopted. Fig. 16(a) exhibits the voltage-capacity curves at the cut-off voltage of 2.3 V, one can see that enhancing D_{O2} substantially contributes to the capacity lift. Also, the discharge plateau is increased. Compared to the base case (D_{O2} =7×10^{-10} m^2/s), the cell voltage plateau rises around 13% for the case of D_{O2} =10×10^{-10} m^2/s. From Fig. 16(b), the specific capacity

and specific energy almost linearly surge with D_{O2}, when improving D_{O2} from 1×10^{-10} to 10×10^{-10} m^2/s, the specific capacity boosts from 132 to 1195 $mAh/g_{\text{-carbon}}$, and the energy density is from 342 to 3093 $mW/g_{\text{-carbon}}$, yielding a growth rate of 800%. The reason can be attributed to the improved oxygen supply for reaction consumption.



(a) (b)

Fig. 16. Effect of D_{O2} on (a) voltage-capacity curve and (b) energy density.



(a) (b)

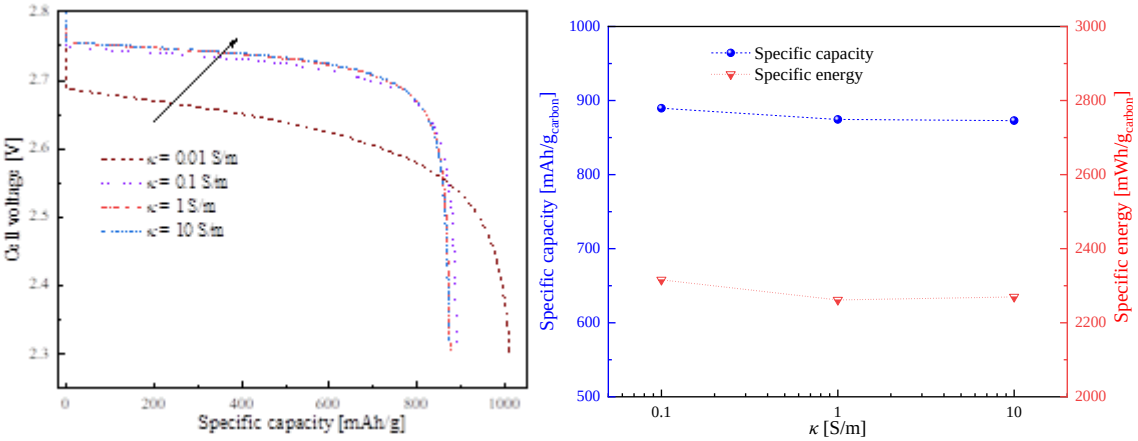
Fig. 17. Effect of D_{O2} on (a) C_{O2} and (b) ε.

Fig. 17(a) and (b) reveal how D_{O2} affects C_{O2} and ε at a fixed SOD. Clearly, the greater D_{O2} leads to a higher C_{O2} at the same position of the cell cathode. In the case of low D_{O2} ($D_{O2}=1\times10^{-10}$ m^2/s), the C_{O2} in the vast majority of the area at the cathode is zero due to the limited mass transfer capability. For the case with high D_{O2} ($D_{O2}=10\times10^{-10}$ m^2/s), the C_{O2} within the cell cathode is maintained above 0.5 mol/m^3, although the C_{O2} near boundary 1 is significantly smaller than that near boundary 2. Fig. 17(b) shows that high D_{O2} is beneficial to the uniformity of porosity distribution within the cathode,

implying that the ORR reaction is occurring at all parts of the cell cathode. However, for the case with low D_{O2}, the ε is the lowest (~0.4) at the position near boundary 2 while it remarkably soars to the highest value (~0.73) with the diminution of dimensionless distance, indicating the ORR reaction only occurs near the cathode/current collector interface.

4.3.3. Effect of electrolyte ionic conductivity

The ionic conductivity of electrolyte κ is one of the crucial indicators that affect the charge/discharge performance of the battery. To study its impact on Li-O_2 batteries discharge behavior, we change κ from 0.01 S/m to 10 S/m. As can be found in Fig. 18(a), upgrading κ from 0.01 S/m to 0.1 S/m, the discharge voltage plateau achieves a distinct lift, from 2.64 V to 2.74 V, meanwhile, the capacity dwindles from 1010.1 mAh/$g_{\text{-carbon}}$ to 889.5 mAh/$g_{\text{-carbon}}$. When κ is further enlarged over 1 S/m, the rise in discharge voltage plateau and the drop in capacity is inconspicuous. As demonstrated in Fig. 18(b), the variation in the specific capacity and specific energy at the range of 0.1 S/m to 10 S/m is extremely small, approximately 873-890 mAh/$g_{\text{-carbon}}$ and 2270-2316 mWh/$g_{\text{-carbon}}$, respectively. The above results enlighten scholars that when the conductivity exceeds 1 S/m, there is no need to excessively pursue the improvement of electrolyte conductivity at the cost of other characteristics. Indeed, the conductivity range of electrolytes currently used in non-aqueous lithium-air batteries is typically between 0.1 and 1.



(a) (b)

Fig. 18. Effect of κ on (a) voltage-capacity curve and (b) energy density.

4.4. Cycling performance

In this part, the cyclability with charge-discharge cycle numbers of Li-O_2 batteries is predicted. The changes in the specific capacity and capacity retention of the cell in 1 M

$LiPF_6$ dissolved in a non-aqueous solvent working between 2.2 V and 4.2 V at a rate of 0.1 mA/cm^2 are elucidated in Fig. 19. As can be seen, the rechargeable Li-O_2 cell is faced the performance deterioration on consecutive discharging-charging cycling. Specifically, the discharge capacity constantly drops to a low value of 322 $mAh/g_{\text{-carbon}}$ from the initial 874 $mAh/g_{\text{-carbon}}$ after 20 cycles, and the corresponding capacity retention is 36.884%. Fortunately, the rate of decline in specific capacity and capacity retention becomes progressively smaller as the number of cycles increases. E.g., the loss of battery capacity during the first ten cycles and the last ten cycles is 43.528% and 19.588%, respectively. The performance degradation in this model is attributed to irreversible electrolyte decomposition. Apart from that, it is affected by the incompletely reversible Li_2O_2 during the recharging process. In practice, the catalytic Li-O_2 batteries are also confronted with efficiency deterioration by other aspects which include the degradation of carbon cathode materials and the formation of other soluble/insoluble products and intermediates. The results highlight the importance of the superior electrolyte to ensure the exceptional performance of Li-O_2 batteries and researchers are still developing efficient Li-O_2 batteries which maintain good cyclability in operation.

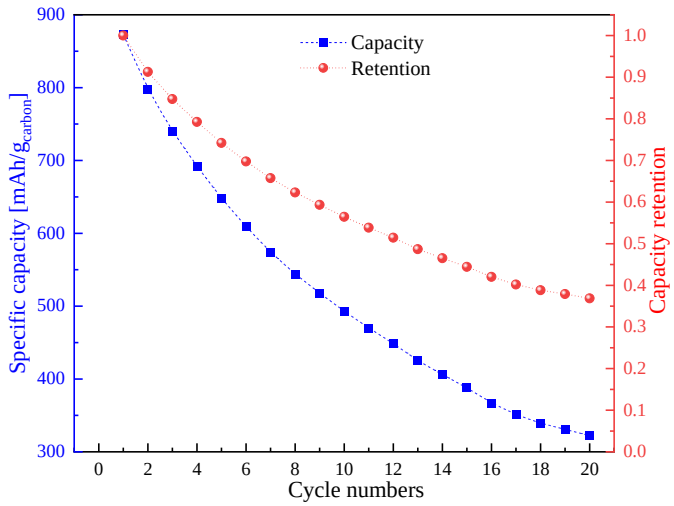


Fig. 19. Variations of discharge capacity and capacity retention against 20 consecutive cycles in this model.

Fig. 20 further discloses the variation of Li_2CO_3 volume fraction inside the cathode with cycle numbers. Obviously, ε_{Li2CO3} presents an upward trend when the cycle number rises, which can be ascribed to the irreversible electrolyte decomposition and the subsequent accumulation of Li_2CO_3 inside the cathode during each discharge. It sharply soars to 6.4% in the first 5 cycles. Although the growth rate of ε_{Li2CO3} gradually slows

down, the rise in ε_{Li2CO3} is still remarkable, escalating from 9.9% to 13.8% as the cycle number elevates from 10 to 20.

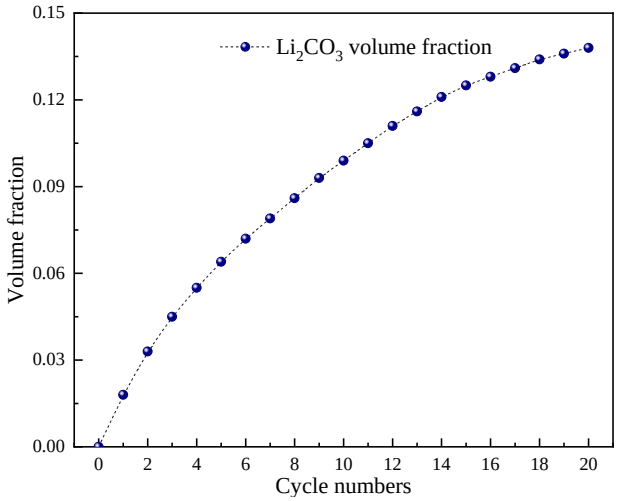


Fig. 20. Volume fraction of Li_2CO_3 formation inside the Li-O_2 cell at the end of each discharge cycle.

5. Conclusions

This article establishes a comprehensive Li-O_2 battery model by simultaneously considering the discontinuous deposit of discharge product Li_2O_2 and the formation of by-product Li_2CO_3 due to electrolyte degradation. The effects of major parameters including operating conditions, properties of electrolyte and electrode, such as oxygen diffusivity and cathode porosity, on discharge characteristics are analyzed in detail based on the proposed model. The following key conclusions can be drawn:

1) Low I_{app} contributes to the specific capacity while the discharge voltage plateau is inversely proportional to I_{app}. Higher I_{app} will cause a faster accumulation of discharge products and a rapid decrease of porosity at the cathode. As discharge depth proceeds, ε_{Li2O2} and ε present an upward trend and downward trend respectively, especially for the position close to the cathode/current collector interface. The effect of regular operating temperature (290 K–330 K) on the discharge behavior is insignificant.

2) When enhancing S_{O2} from 0.2 to 1, the voltage plateau rises from 2.68 V to 2.77 V, and the capacity extends from 449.9 mAh/$g_{\text{-carbon}}$ to 1532.1 mAh/$g_{\text{-carbon}}$, achieving a 240.5% increase due to the intensified reaction kinetics. Similarly, energy density almost linearly surges with D_{O2} thanks to the improved O_2 transport and supply for reaction consumption. Boosting κ from 0.01 S/m to 0.1 S/m can substantially elevate discharge

plateau but the promotion will be inconspicuous once κ is further enlarged over 1 S/m.

3) Improved catalytic reactivity k_c is conducive to the discharge voltage and specific energy. With the rise of ε from 0.73 (base case) to 0.93, the specific capacity is enlarged from 874 to 6122 mAh/$g_{\text{-carbon}}$, and the corresponding specific energy upgrades from 2259.8 to 15610 mWh/$g_{\text{-carbon}}$. Shortening cathode thickness facilitates the efficient utilization of carbon cathode material but this comes at the expense of lowering the mass loading of carbon, as L_{ca} reduces from 750 μm to 100 μm, the specific capacity and energy surge to 2740.3 mAh/$g_{\text{-carbon}}$ and 6868.6 mWh/$g_{\text{-carbon}}$, respectively. Nevertheless, the practical energy yields a 59.4% drop.

4) The capacity constantly declines to 322 mAh/$g_{\text{-carbon}}$ from the initial 874 mAh/$g_{\text{-carbon}}$ after 20 consecutive charge-discharge cycles, and the corresponding capacity retention is 36.884%, accompanied by a 13.8% volume fraction of Li_2CO_3 formation inside the cathode.

Overall, this research may offer guidance in designing electrodes and electrolytes for the recently developed Li-O_2 batteries and provide an energy conversion behavior prediction and performance regulation strategy.

Acknowledgments

This work was supported by the Natural Science Foundation of Jiangsu Province (No. BK20230319) and the National Natural Science Foundation of China (No. 52176085).

Author contributions

Wei Li: Conceptualization, Methodology, Investigation, Modelling, Software, Data curation, Formal analysis, Writing- Original draft, Writing - Review & Editing; **Min Zeng:** Project administration, Funding acquisition, Resources; **Bohong Wang:** Investigation, Writing - Review & Editing; **Yujie Chen:** Validation, Writing - Review & Editing; **Christos N. Markides:** Writing -Review & Editing.

References

[1] Li W, Zhang L, Ling X. Thermo-economic assessment of salt hydrate-based thermochemical heat transformer system: Heat upgrade for matching domestic hot water production. Energy

Conversion and Management 2023;277:116644.
[2] Gul E, Baldinelli G, Bartocci P, Shamim T, Domenighini P, Cotana F et al. Transition toward net zero emissions - Integration and optimization of renewable energy sources: Solar, hydro, and biomass with the local grid station in central Italy. Renewable Energy 2023;207:672–86.
[3] Vérez D, Borri E, Zsembinszki G, Cabeza LF. Thermal energy storage co-benefits in building applications transferred from a renewable energy perspective. Journal of Energy Storage 2023;58:106344.
[4] Crespo A, Fernández C, Vérez D, Tarragona J, Borri E, Frazzica A et al. Thermal performance assessment and control optimization of a solar-driven seasonal sorption storage system for residential application. Energy 2023;263:125382.
[5] Li Y, Lu J. Metal–Air Batteries: Will They Be the Future Electrochemical Energy Storage Device of Choice? ACS Energy Lett. 2017;2(6):1370–7.
[6] Zhang Z, Xiao X, Zhu X, Tan P. Addressing Transport Issues in Non-Aqueous Li–air Batteries to Achieving High Electrochemical Performance. Electrochem. Energy Rev. 2023;6(1).
[7] Qiu Q, Long J, Yao P, Wang J, Li X, Pan Z-Z et al. Cathode electrocatalyst in aprotic lithium oxygen (Li-O2) battery: A literature survey. Catalysis Today 2023;420:114138.
[8] Kim JG, Noh Y, Kim Y. Pyrochlore LaSrSn2O7 nanoparticles anchored on carbon nanofibers as bifunctional catalysts for an efficient Li-O2 battery. Journal of Energy Storage 2023;66:107329.
[9] Dou W, Cheng Z, Zhang X, Duan J, Sun Z, Lei J et al. Intelligently tuning the electronic structure of solid catalyst for bidirectional electrode process in lithium-oxygen batteries. Cell Reports Physical Science 2023;4(6):101448.
[10] Lv H, Fan C, Xu X, Zhao C, Long J. Design of chromium-doped spinel Mn3O4 modulated electronic structure as an efficient catalyst for Li-O2 batteries. Journal of Alloys and Compounds 2023;953:170130.
[11] Wang L, Lu Y, Xie M, Zhao S, Li Z, Liu Q. Interfacially engineered induced nickel-based heterostructures as efficient catalysts for Li-O2 batteries. Electrochimica Acta 2023;437:141476.
[12] Alaf M, Tocoglu U, Kartal M, Akbulut H. Graphene supported heterogeneous catalysts for Li–O2 batteries. Applied Surface Science 2016;380:185–92.
[13] Guo S, Wang J, Sun Y, Peng L, Li C. Interface engineering of Co3O4/CeO2 heterostructure in-situ embedded in Co/N-doped carbon nanofibers integrating oxygen vacancies as effective oxygen cathode catalyst for Li-O2 battery. Chemical Engineering Journal 2023;452:139317.
[14] Liang R, Shu C, Hu A, Li M, Ran Z, Zheng R et al. Interface engineering induced selenide lattice distortion boosting catalytic activity of heterogeneous CoSe2@NiSe2 for lithium-oxygen battery. Chemical Engineering Journal 2020;393:124592.
[15] Sung M-C, Lee G-H, Kim D-W. Efficient Li2O2 oxidation kinetics of perovskite-type lanthanum chromium-based oxide by promoter interface formation for lithium-oxygen batteries. Energy Storage Materials 2023;60:102829.
[16] Sun C, Xiao F, Di Wu, Lian G, Cui D, Wang Q et al. Co nanoparticles embedded into leaf-like porous carbon as a promising cathode catalyst for Li-O2 batteries. Journal of Electroanalytical Chemistry 2023;944:117663.
[17] Hou C, Han J, Liu P, Yang C, Huang G, Fujita T et al. Operando observations of RuO2 catalyzed Li2O2 formation and decomposition in a Li-O2 micro-battery. Nano Energy 2018;47:427–33.
[18] Cao D, Zheng L, Wang Y, Dong Y, Li Q, Li Y et al. Ultraviolet-assisted construction of low-Pt-loaded MXene catalysts for high-performance Li−O2 batteries. Energy Storage Materials

2022;51:806–14.
[19] Sun G, Zhang Z, Yang D, Wang Y, Lu W, Liu M et al. The effect of AlF3 as an electrolyte additive on Li anode in Li-O2 batteries. Journal of Alloys and Compounds 2023;952:169971.
[20] Gong L, Chen M, Tang Z, Chen Q, Zhang J, Hou G et al. Carbon-sulfur double bond electrolyte additives as redox mediator for lithium-oxygen batteries. Surfaces and Interfaces 2023;39:102867.
[21] Lee J-S, Shin K, Jun S-Y, Kim S, Ryu W-H. Dual-functional vinylpyrrolidone electrolyte additive as anode surface leveler and cathode catalyst for lithium Metal-Oxygen batteries. Chemical Engineering Journal 2023;458:141383.
[22] Kondori A, Esmaeilirad M, Harzandi AM, Amine R, Saray MT, Yu L et al. A room temperature rechargeable Li_2O-based lithium-air battery enabled by a solid electrolyte. Science 2023;379(6631):499–505.
[23] Zhang B, Ju Z, Xie Q, Luo J, Du L, Zhang C et al. Ti3CNTx MXene/rGO scaffolds directing the formation of a robust, layered SEI toward high-rate and long-cycle lithium metal batteries. Energy Storage Materials 2023;58:322–31.
[24] Huang Z, Ren J, Zhang W, Xie M, Li Y, Sun D et al. Protecting the Li-Metal Anode in a Li–O2 Battery by using Boric Acid as an SEI-Forming Additive. Adv. Mater. 2018;30(39):1803270.
[25] Lee DJ, Lee H, Kim Y-J, Park J-K, Kim H-T. Sustainable Redox Mediation for Lithium–Oxygen Batteries by a Composite Protective Layer on the Lithium-Metal Anode. Adv. Mater. 2016;28(5):857–63.
[26] Amici J, Alidoost M, Francia C, Bodoardo S, Martinez Crespiera S, Amantia D et al. O2 selective membranes based on a dextrin-nanosponge (NS) in a PVDF-HFP polymer matrix for Li–air cells. Chemical Communications 2016;52(94):13683–6.
[27] Sahapatsombut U, Cheng H, Scott K. Modelling of operation of a lithium-air battery with ambient air and oxygen-selective membrane. Journal of Power Sources 2014;249:418–30.
[28] Ko Y, Kim H-I, Cho S-J, Lee KM, Jung GY, Park H et al. Liquid-Based Janus Electrolyte for Sustainable Redox Mediation in Lithium–Oxygen Batteries. Adv. Energy Mater. 2021;11(38):2102096.
[29] Matsuda S, Ono M, Asahina H, Kimura S, Mizuki E, Yasukawa E et al. Chemical Crossover Accelerates Degradation of Lithium Electrode in High Energy Density Rechargeable Lithium–Oxygen Batteries. Adv. Energy Mater. 2023;13(11):2203062.
[30] Xu Z, Liu Z, Gu Z, Zhao X, Guo D, Yao X. Polyimide-Based Solid-State Gel Polymer Electrolyte for Lithium–Oxygen Batteries with a Long-Cycling Life. ACS Applied Materials & Interfaces 2023;15(5):7014–22.
[31] Song M, Tian C, Huang T, Yu A. Hybrid Ceramic-Gel Polymer Electrolyte with a 3D Cross-Linked Polymer Network for Lithium–Oxygen Batteries. ACS Applied Energy Materials 2023;6(14):7681–91.
[32] Sahapatsombut U, Cheng H, Scott K. Modelling the micro–macro homogeneous cycling behaviour of a lithium–air battery. Journal of Power Sources 2013;227:243–53.
[33] Sahapatsombut U, Cheng H, Scott K. Modelling of electrolyte degradation and cycling behaviour in a lithium–air battery. Journal of Power Sources 2013;243:409–18.
[34] Gwak G, Ju H. Three-dimensional transient modeling of a non-aqueous electrolyte lithium-air battery. Electrochimica Acta 2016;201:395–409.
[35] Tan P, Ni M, Shao Z, Chen B, Kong W. Numerical investigation of a non-aqueous lithium-oxygen

battery based on lithium superoxide as the discharge product. Applied Energy 2017;203:254–66.
[36] Jung CY, Zhao TS, An L. Modeling of lithium–oxygen batteries with the discharge product treated as a discontinuous deposit layer. Journal of Power Sources 2015;273:440–7.
[37] Radin MD, Rodriguez JF, Tian F, Siegel DJ. Lithium Peroxide Surfaces Are Metallic, While Lithium Oxide Surfaces Are Not. Journal of the American Chemical Society 2012;134(2):1093–103.
[38] Adams BD, Radtke C, Black R, Trudeau ML, Zaghib K, Nazar LF. Current density dependence of peroxide formation in the Li–O2 battery and its effect on charge. Energy & Environmental Science 2013;6(6):1772–8.
[39] Zhai D, Wang H-H, Yang J, Lau KC, Li K, Amine K et al. Disproportionation in Li–O2 Batteries Based on a Large Surface Area Carbon Cathode. Journal of the American Chemical Society 2013;135(41):15364–72.
[40] Freunberger SA, Chen Y, Drewett NE, Hardwick LJ, Bardé F, Bruce PG. The Lithium–Oxygen Battery with Ether-Based Electrolytes. Angew. Chem. Int. Ed. 2011;50(37):8609–13.
[41] Wang Y, Hao L, Bai M. Modeling the multi-step discharge and charge reaction mechanisms of non-aqueous Li-O2 batteries. Applied Energy 2022;317:119189.
[42] Li W, Zhang L, Klemeš JJ, Wang Q, Zeng M. Thermochemical energy conversion behaviour in the corrugated heat storage unit with porous metal support. Energy 2022;259:124966.
[43] Read J. Characterization of the Lithium/Oxygen Organic Electrolyte Battery. Journal of The Electrochemical Society 2002;149(9):A1190.